THE JOURNAL OF PHYSICAL CHEMISTRY LETTERS
A JOURNAL OF THE AMERICAN CHEMICAL SOCIETY

pubs.acs.org/JPCL

Letter

Competing Energy Transfer-Modulated Dual Emission in Mn^{2+}-Doped $Cs_2NaTbCl_6$ Rare-Earth Double Perovskites

Yuanjie Chen, Ruosheng Zeng,* Qilin Wei, Shuai Zhang, Binbin Luo, Canxu Chen, Xiaoshan Zhu, Sheng Cao, Bingsuo Zou, and Jin Zhong Zhang*

Cite This: J. Phys. Chem. Lett. 2022, 13, 8529−8536

Read Online

ACCESS | Metrics & More | Article Recommendations | Supporting Information

ABSTRACT: $A_2B^IB^{III}X_6$ double perovskites are promising materials due to their outstanding photoelectronic properties and excellent stability in the environment. Herein, we synthesized Mn^{2+}:$Cs_2NaTbCl_6$ with dual emission through a solvothermal method for the first time. Mn^{2+}:$Cs_2NaTbCl_6$ double perovskites exhibit excellent environmental stability and high photoluminescence quantum yields (PLQYs). The $Cs_2NaTbCl_6$ was successfully doped with Mn^{2+} in two modes: at Mn-feeding concentrations below 1%, Mn^{2+} first tend to insert into the interstitial void, but if the Mn-feeding concentration exceeds 1%, Mn^{2+} will further substitute Na^+ site of the $Cs_2NaTbCl_6$ lattice and thus both two doping modes coexist. After Mn^{2+} doping, efficient energy transfer from the $^5D_4$ level of Tb^{3+} ions to the $^4T_1$ level of Mn^{2+} ions occurs, resulting in tunable dual emission from the Tb^{3+} $^5D_4 \rightarrow {}^7F_{J=6,5,4,3}$ transition and Mn^{2+} $^4T_1 \rightarrow {}^6A_1$ transition. Further, LED based on the Mn^{2+}:$Cs_2NaTbCl_6$ double perovskites exhibits excellent performance and stability. This work demonstrates a strategy to achieve novel lanthanide-based double perovskites with potential applications in photonics.

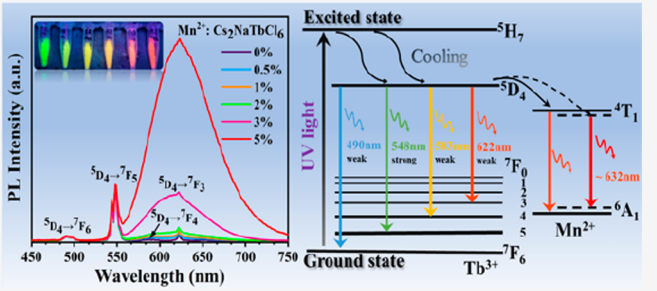

Lead halide perovskites of ABX_3 (A = MA^+, Cs^+; B = Pb^{2+}, X = Cl^-, Br^-, I^-) have been widely studied due to their promising optoelectronic applications such as such as solar cells,[1−3] light-emitting diodes,[4−7] lasers,[8−10] X-ray detectors,[11−13] and scintillators.[14,15] However, lead-based halide perovskites are often unstable and easily hydrolyzed.[16−18] Meanwhile, the toxicity of lead limits their applications.[19] Thus, it is urgent to develop alternative lead-free perovskites with photoelectric properties similar to those of lead-based perovskites.

To date, there are two main methods to synthesize lead-free halide materials.[20,21] The first is to replace Pb^{2+} ions with the same family elements such as Sn^{2+} and Ge^{2+}. Because of their same ns^2 electronic configuration as that of Pb^{2+} ions,[22,23] these elements ensure the excellent photoelectric properties of the perovskites, and with lower toxicity. However, Sn^{2+} and Ge^{2+} ions without $6s^2$ lone-pair states are easily oxidized,[24−26] resulting in the deterioration of the samples. Another method is to replace lead with other benign elements with ns^2 electronic configuration, e.g., Bi^{3+} and In^{3+}.[27] However, such a replacement would cause a reduction in dimensionality and charge imbalance if only the trivalent ions are used.[28−30] Based on isoelectronic theory, this issue can be addressed by using a proper monovalent cation in conjunction with trivalent ions to generate double perovskites $A_2M^IM^{III}X_6$ (A = Cs; M^I = Na, K, Ag; M^{III} = Bi, In, and Sb, and X = Cl, Br, I). However, most lead-free double perovskites exhibit low photoluminescence (PL) due to indirect bandgap or parity forbidden transitions.[31−34] Through appropriate ion doping or alloying, the bandgap of double perovskites can be altered or their structural symmetry can be broken, which can break the partial forbidden transition and thereby enhance their optical properties.[35,36] Various dopants, such as Sb^{3+}, Mn^{2+}, and Ln^{3+}, have been studied for doping double perovskites.[37−42]

Lanthanide ions have a rich $4f^n$ electron configuration and possess the shielding effect of the outermost $5s^25p^6$ full-layer electrons. They exhibit rich and unique spectral properties with relatively sharp spectral line widths, which are relatively insensitive to the environment.[43,44] Thus, rare-earth doped double perovskites have attracted more attention. For instance, Chen et al. successfully synthesized Yb^{3+}:Cs_2AgBiX_6 (X = Cl^-, Br^-) nanocrystals (NCs) by a hot injection method.[45] In addition to the inherent visible emission (trap state emission), a new near-infrared (NIR) emission attributed to $^2F_{5/2} \rightarrow {}^2F_{7/2}$ f−f transition of Yb^{3+} ions was observed for the doped double perovskite NCs. Arfin et al. reported that Bi^{3+}/Er^{3+} codoped $Cs_2AgInCl_6$ powder showed a broad self-trapped exciton (STE) emission at about 600 nm, a 552 nm band attributed to

Received: August 10, 2022
Accepted: September 1, 2022
Published: September 6, 2022

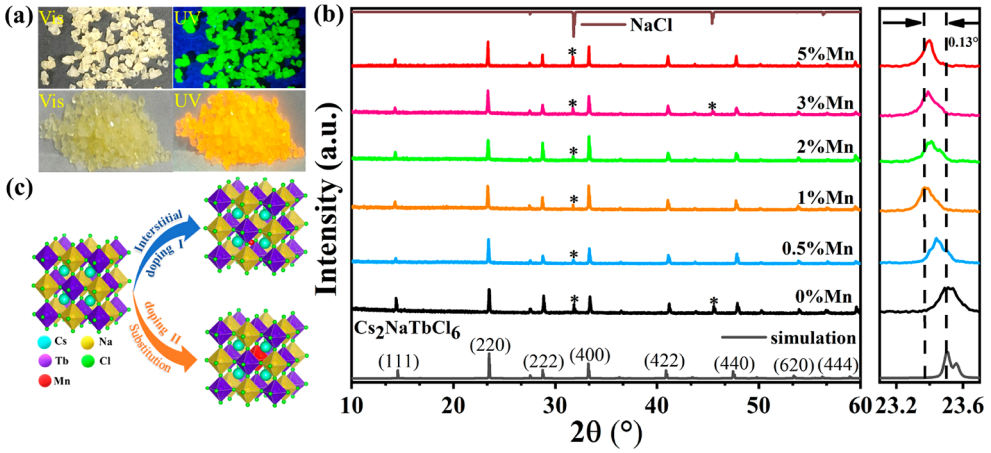

Figure 1. (a) Digital photographs of pristine (upper panel) and Mn:$Cs_2NaTbCl_6$ (lower panel) crystals under visible or 302 nm-UV light. (b) XRD patterns of Mn:$Cs_2NaTbCl_6$ with different Mn^{2+}-feeding concentrations. (c) Schematic illustration for two possible modes of doping of Mn^{2+}-doped $Cs_2NaTbCl_6$.

the $^4S_{3/2} \rightarrow {}^4I_{15/2}$ transition of Er^{3+} ions, a 660 nm emission band assigned to the $^4F_{9/2} \rightarrow {}^4I_{15/2}$ transition of Er^{3+} ions, and infrared emission at 1540 nm due to the $^4I_{13/2} \rightarrow {}^4I_{15/2}$ transition of Er^{3+} ions.[46] These lead-free double perovskites were doped with lanthanide ions to achieve the PL properties in the infrared region. Doping rare-earth ions can also improve the PL properties in the visible region. Xia's group reported $Cs_2Ag(In_{1-x}Tb_x)Cl_6$:Bi NCs with emission tuned from green to orange by modulating the Tb^{3+}-doping concentration.[44] Mn^{2+} is also a typical ion that can modulate luminescence of semiconductors. However, the incorporation of Mn into rare-earth based hosts has been rare, and possible effect on optical properties is not yet clear.

In this work, Mn^{2+}-doped rare-earth $Cs_2NaTbCl_6$ double perovskites with dual emission were synthesized through a solvothermal method. The optical properties of the Mn^{2+}:$Cs_2NaTbCl_6$ rare-earth double perovskites were modulated by changing the Mn^{2+}-feeding concentration while keeping the crystal structure unchanged. Meanwhile, the doping sites of the Mn^{2+} ions were determined through a combined experimental and theoretical studies. The Mn^{2+} doping introduces a new emission channel, and the emission color changes continuously from green to red with increasing Mn^{2+}-feeding concentration. A model is proposed to explain the related physical processes in terms of competitive energy transfer pathways.

Figure 1a shows photographs of undoped and 3%Mn^{2+}-doped $Cs_2NaTbCl_6$ samples. The undoped sample exhibits green emission under excitation at 302 nm but the 3%Mn^{2+}-doped sample emits orange light. Figure S10 shows Mn^{2+}-doped $Cs_2NaTbCl_6$ is of high-quality single crystals (SCs). Figure 1b shows the XRD patterns of x%Mn:$Cs_2NaTbCl_6$ (x = 0, 0.5, 1, 2, 3, 5). The XRD peaks are consistent with the standard card ICSD #96062, demonstrating that all the synthesized microcrystals are cubic phase adopting a cubic space group $Fm\bar{3}m$ with a lattice parameter of around 10.94 Å, and the samples have good crystallinity. However, some NaCl reflection peaks appear at 31.79° and 45.39°, indicating that the feeding amount of 1.00 mmol NaCl is of slight overdose.[47] The (220) plane for the doped sample diffraction peak first shifts toward lower angles and reaches a maximum of 0.13° at 1%Mn^{2+}-feeding concentration, then shift back a little when the Mn^{2+}-feeding concentration further increases. This peak shift indicates that Mn^{2+} ions are effectively introduced into the $Cs_2NaTbCl_6$ lattice, and the lattice volume first gradually increases and then slightly decreases as Mn^{2+}-feeding concentration increases. The ionic radius of Mn^{2+} (0.83 Å) is smaller than those of Cs^+ (1.88 Å), Na^+ (1.02 Å), and Tb^{3+} (0.923 Å); thus, we infer that Mn^{2+} ions not only are inserted into the interstitial void of the $Cs_2NaTbCl_6$ but also may substitute the Na^+ or Tb^{3+} sites when the Mn^{2+}-feeding concentration exceeds 1%. Figure 1c shows a schematic diagram for the proposed structural change with doping.

To help with understanding of the doping mechanism of Mn^{2+}, first-principles calculations were conducted to simulate the corresponding formation energy as well as the stability of the defect systems of Mn^{2+} ions in the $Cs_2NaTbCl_6$ host lattice. Figure 2a–f show the relaxed structure of Mn:$Cs_2NaTbCl_6$ under six possible doping conditions. Among them, Figure 2a–c represent the substitution of Mn at Cs, Na, and Tb sites in a single form, respectively. Meanwhile, Figure 2d shows the interstitial doping; we choose the way that Mn^{2+} is inserted in the interstitial void between Cs–Cs and Cl–Cl because this structure with such an interstitial doping is the most stable. Figure 2e and f show the coexistence of interstitial and substitutional doping at Na or Tb sites, respectively. The above doping conditions are modeled in supercell $Cs_2NaTbCl_6$, and the corresponding formation energy is calculated using the following equation: $\Delta E(\alpha) = E(\alpha) - E(perfect) + \Sigma_i n_i \Delta\mu_i$.[48] More details about the calculation method are described in the Supporting Information.

All formation energies under different doping conditions are graphically shown in Figure 2g. Conditions a and c have positive formation energies, indicating that it is unfavorable for Mn^{2+} to substitute for Cs^+ and Tb^{3+} in a single metal ion occupied position. Condition b has a negative formation energy of −0.40 eV, indicating that it is favorable for Mn^{2+} to substitute for Na^+. Condition d has lower formation energy of −1.72 eV, indicating that it is highly preferable to dope $Cs_2NaTbCl_6$ with Mn^{2+} interstitially. Then the simultaneous existence of substitutional and interstitial doping (conditions e and f) is calculated. Condition e shows the lowest formation energy of −2.15 eV, indicating that it is much more preferable for Mn^{2+} to occupy the interstitial lattice sites and simultaneously substitute the Na^+ sites. On the contrary,

https://doi.org/10.1021/acs.jpclett.2c02491
J. Phys. Chem. Lett. 2022, 13, 8529−8536

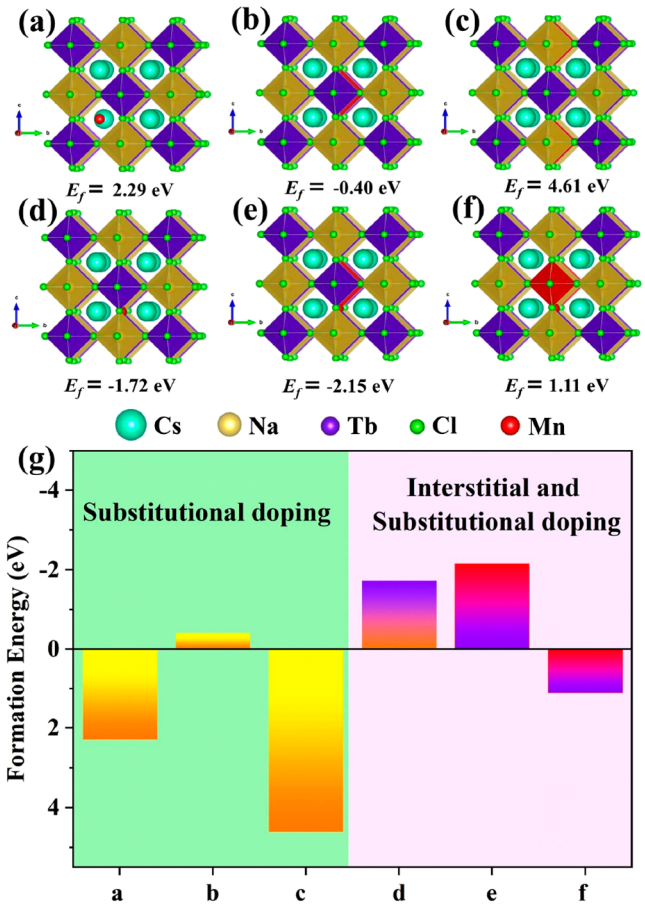

Figure 2. Relaxed structures of possible different Mn^{2+} doping conditions in the $Cs_2NaTbCl_6$ host. Substitutional doping of Mn at (a) Cs, (b) Na, and (c) Tb site, respectively. (d) Doping of Mn in the interstitial void. The coexistence of interstitial and substitutional doping at (e) Na or (f) Tb sites, respectively. (g) According formation energies for different Mn^{2+} doping conditions.

condition f has positive formation energy, indicating that it is inappropriate for Mn^{2+} to occupy the interstitial lattice sites and concurrently substitute the Tb^{3+} sites. Therefore, the most appropriate way for Mn^{2+} ions to enter into the crystalline lattice is that first inclined to insert into the interstitial void. When the interstitial doping is saturated, the Mn^{2+} ions will substitute the Na^+ sites rather than Tb^{3+} sites. The theoretical calculation is consistent with the XRD results.

XPS analyses were carried out to further confirm the presence of Mn^{2+} in the Mn:$Cs_2NaTbCl_6$ (Figure S1a–e). In Figure S1a, the peaks at 738.8 and 724.9 eV are attributed to the Cs $3d_{3/2}$ and $3d_{5/2}$ orbitals, respectively. Figure S1b shows the peak of the Na 1S orbital, which is located at 1071.3 eV before doping and then shifts to higher energies by 1.4 eV after doping. In Figure S1c, the peaks of Tb $3d_{3/2}$ and $3d_{5/2}$ can be clearly observed, which shift from 1277.7 and 1242.7 eV to 1279.9 and 1244.9 eV, respectively. In Figure S1d, the two peaks at 199.5 and 197.8 eV are attributed to the Cl $2p_{1/2}$ and $2p_{3/2}$ orbitals, respectively. The characteristic diffraction peak at 652.3 eV of Mn is observed in Figure S1e. The peaks of Cs 3d and Cl 2p do not shift after doping. However, the binding energies of Na 1s and Tb 3d slightly shift to higher energy. We suggest that both interstitial doping of Mn^{2+} and substitutional doping at Na^+ site are present in the doped system, which results in the distortion of $[TbCl_6]^{3-}$ and $[NaCl_6]^{5-}$ octahedrons and thereby shift of the orbital energy of Tb and Na toward high energy.

Figure S2 shows the energy dispersive spectrum (EDS) of 5%Mn:$Cs_2NaTbCl_6$, which reveals uniform distribution of Cs, Na, Tb, Cl, and Mn elements. The atomic ratio of Cs:Na:Tb:Cl is approximately consistent with the stoichiometric ratio of $Cs_2NaTbCl_6$. And the actual elemental content of Mn is about 2.9%, while the Mn^{2+}-feeding concentration is 5%.

The influence of Mn^{2+} doping on the electronic band structure was investigated by density functional theory (DFT) calculations. Figure S3a shows the band structure and DOS of the undoped $Cs_2NaTbCl_6$, where the maximum valence band (VBM) is mainly composed of Cl p orbitals, and the minimum conduction band (CBM) is mainly composed of Tb s orbitals and Cl p orbitals. Figures S3b–d show the energy band structures and DOS of substitution of the Na^+ sites by Mn^{2+}, interstitial doping with Mn, and coexistence of both substitutional and interstitial doping, respectively. While the VBM is not changed significantly, Mn s and d orbits are observed at the CBM. However, Mn^{2+} doping leads to some additional states in the forbidden bandgap of $Cs_2NaTbCl_6$ due to the Mn 3d orbitals, which may facilitate energy transfer and d–d transition in Mn^{2+}.

Figure 3a shows the absorption spectra of 0–5% Mn:$Cs_2NaTbCl_6$. The absorption coefficient gradually increases as Mn^{2+}-feeding concentration increases. The absorption peak at ~278 nm is attributed to the $4f^8 \rightarrow 4f^75d^1$ transition of Tb^{3+}, while the peaks around 300–520 nm are attributed to the 4f → 4f transition of Tb^{3+} and $^6A_1 \rightarrow {}^4E$, $^6A_1 \rightarrow {}^4T_{1,2}$, and $^6A_1 \rightarrow {}^4A_1$ transitions of Mn^{2+}, which overlap. Figure S4b show the PLE and absorption spectra of 3% Mn:$Cs_2NaTbCl_6$. The position of the excitation bands matches well with the absorption bands, and the excitation bands at 225–300 nm are due to the host. The excitation bands at 300–400 nm are from Tb^{3+} and Mn^{2+}. Figure S4c shows the PLE spectra of 0%, 3%, and 5%Mn:$Cs_2NaTbCl_6$, which are similar in profile at 548 and 622 nm. While the intensity of the 278 nm PLE band monitored at 548 nm emission gradually decreases, the intensity of the 278 nm PLE band monitored at 622 nm emission gradually increases as the Mn^{2+}-feeding concentration increases. Such changes indicate possible competition in energy transfer pathways in the Mn-doped $Cs_2NaTbCl_6$.

Figure S4a shows the PL spectra of undoped $Cs_2NaTbCl_6$ that exhibit four sharp emission bands at 490, 548, 583, and 622 nm, which are attributed to the $^5D_4 \rightarrow {}^7F_{J=6,5,4,3}$ transitions of Tb^{3+}, respectively. The strongest emission at 548 nm originates from the $^5D_4 \rightarrow {}^7F_5$ transition, and other weak emissions at 490, 583, and 622 nm are attributed to the transitions of $^5D_4 \rightarrow {}^7F_6$, $^7F_4$, and $^7F_3$, respectively. As shown in Figure 3d, after Mn^{2+} ions are introduced, characteristic emission of Mn^{2+} at 622 nm originating from the $^4T_1 \rightarrow {}^6A_1$ transition appears. By normalizing the intensity of PL peak at 548 nm, the PL intensity at 622 nm is gradually enhanced with increasing Mn^{2+}-feeding concentration. The double peaks integration ratios $S_{622\ nm}/S_{548\ nm}$ are shown in Figure 3b (black curve), and the positive correlation with the Mn^{2+}-feeding concentration indicates that the energy transfer from $^5D_4$ of Tb^{3+} to $^4T_1$ of Mn^{2+} is promoted. As shown in Figure 3b (red curve), the intrinsic PL intensity at 548 nm first increases and then gradually decreases as the Mn^{2+}-feeding concentration increases. This indicates that an energy transfer process from

https://doi.org/10.1021/acs.jpclett.2c02491
J. Phys. Chem. Lett. 2022, 13, 8529–8536

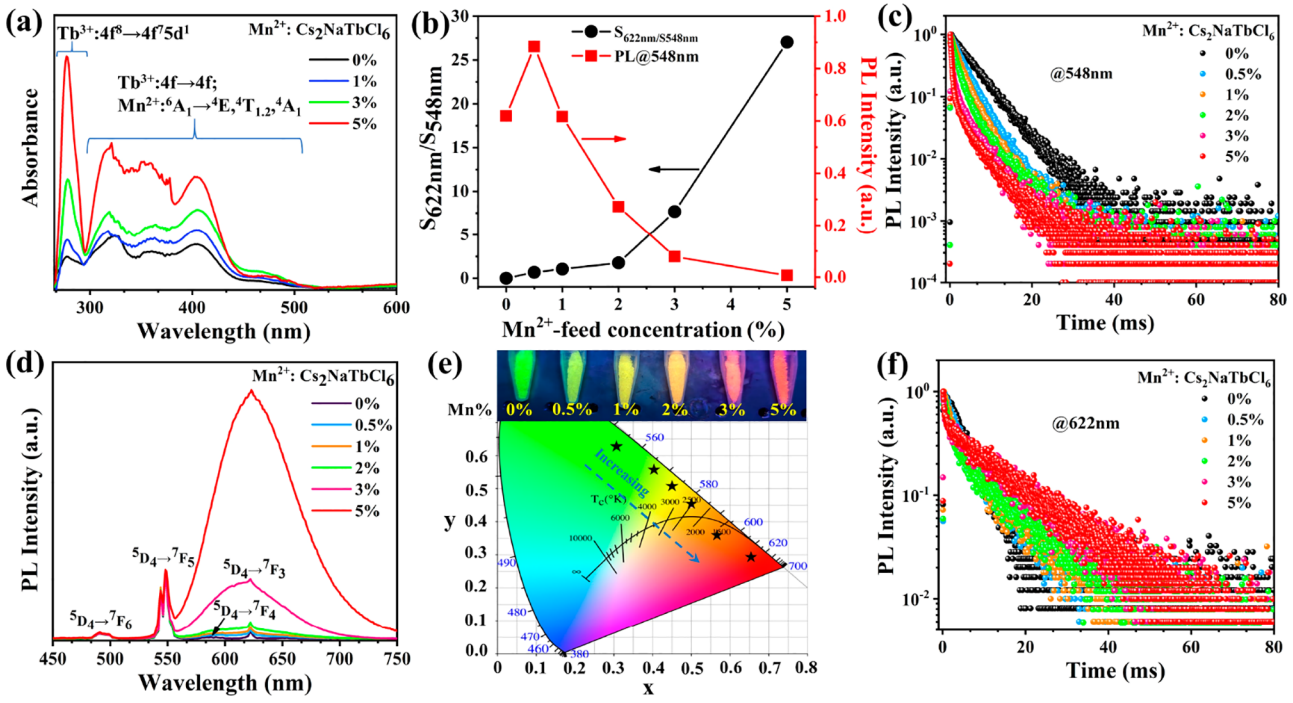

Figure 3. (a) Absorption spectra of $Cs_2NaTbCl_6$ crystals with different Mn^{2+}-feeding concentrations. (b) Integral ratio of the double emission $S_{622\ nm}/S_{548\ nm}$ (black) and 548 nm PL intensity (red) of $Cs_2NaTbCl_6$ crystals with different Mn^{2+}-feeding concentrations. (c) PL decay curves (λ_{ex} = 278 nm, λ_{em} = 548 nm) of $Cs_2NaTbCl_6$ with different Mn^{2+}-feeding concentrations. (d) Normalized PL spectra of $Cs_2NaTbCl_6$ crystals with different Mn^{2+}-feeding concentrations under 278 nm excitation. (e) CIE color coordinates and photos of the as-prepared Mn:$Cs_2NaTbCl_6$ samples under an UV lamp. (f) PL decay curves (λ_{ex} = 278 nm, λ_{em} = 622 nm) of $Cs_2NaTbCl_6$ with different Mn^{2+}-feeding concentrations.

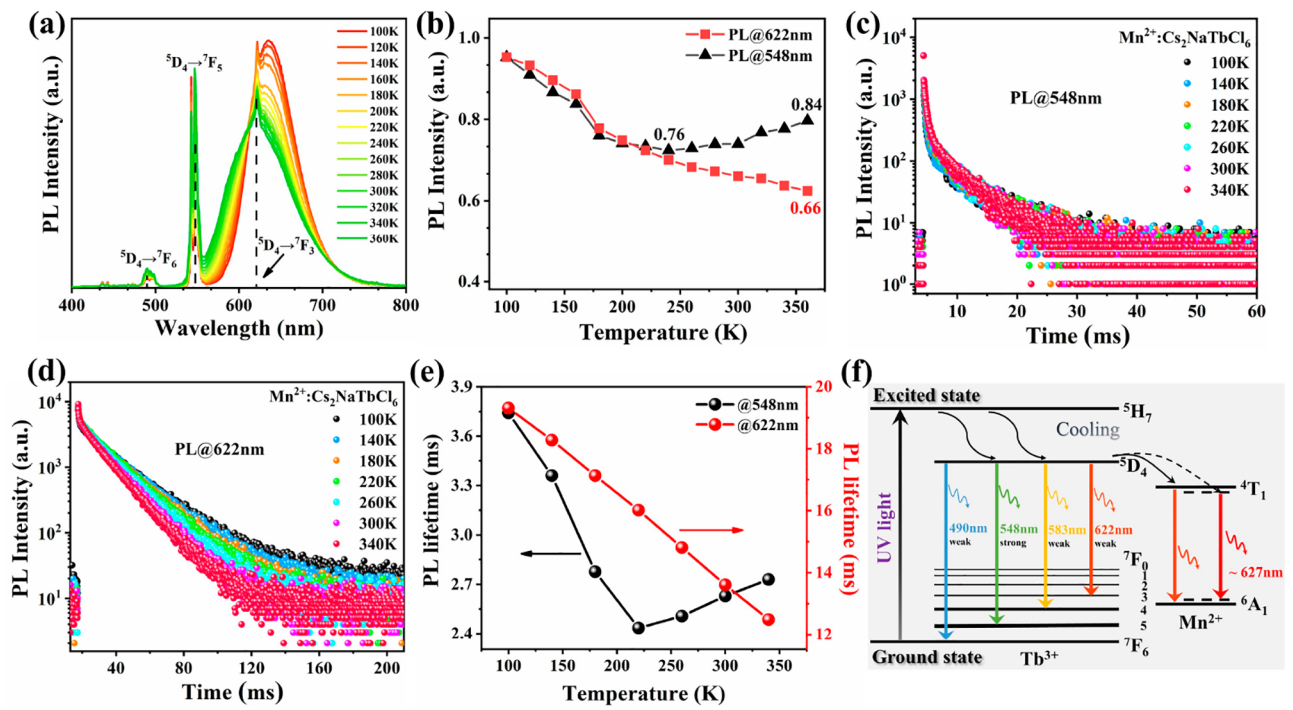

Figure 4. (a) Temperature-dependent PL spectra of 3%Mn:$Cs_2NaTbCl_6$. (b) Evolution of intensity of PL peaks at 548 and 622 nm at different temperatures. Time-resolved PL decay curves of 3%Mn:$Cs_2NaTbCl_6$ with emission at (c) 548 and (d) 622 nm at different temperatures. (e) Evolution of PL lifetimes at 548 and 622 nm emission. (f) Schematic illustration of photoexcited emission processes in Mn-doped $Cs_2NaTbCl_6$.

Tb to Mn probably exists. The theoretical calculations show that although $Cs_2NaTbCl_6$ has a direct bandgap (Figure S5), the Γ point in the first Brillouin zone is parity-forbidden for the $\Gamma_4^+ \rightarrow \times\Gamma_5^+$ transition; thus, weak or no radiative recombination is expected. However, with incorporation of Mn^{2+} ions, the structural symmetry is broken and the electrons are highly localized around Mn, which breaks the inherent parity and forbidden transition and results in effective energy transfer

https://doi.org/10.1021/acs.jpclett.2c02491
J. Phys. Chem. Lett. 2022, 13, 8529−8536

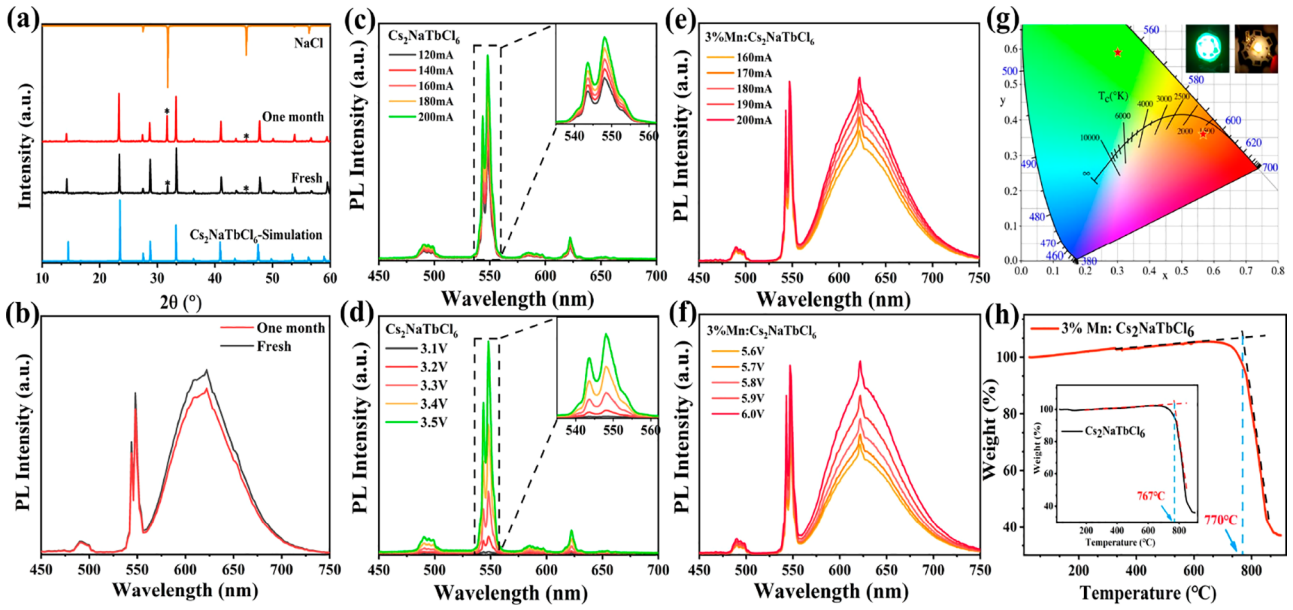

Figure 5. (a) XRD patterns and (b) PL of 3%Mn:$Cs_2NaTbCl_6$ stored in the air for one month to test the material stability. Corresponding emission spectra of LED based on (c, d) pristine $Cs_2NaTbCl_6$ and (e, f) 3%Mn:$Cs_2NaTbCl_6$ under different voltages and currents. (g) CIE coordinates of green and orange LEDs (insets are the working photos of the devices). (h) Thermogravimetric analysis of pristine $Cs_2NaTbCl_6$ (inset) and 3%Mn:$Cs_2NaTbCl_6$.

from Tb^{3+} to Mn^{2+} and enhanced luminescence at 548 nm. The intensity of the intrinsic PL peak at 548 nm decreases with excessing 0.5% Mn^{2+}-feeding concentration, which is attributed to concentration quenching or spin−orbit coupling interaction between Mn and Tb or between Mn−Mn pairs. In Figure 3e, depending on the Mn^{2+}-doping concentration, the CIE colors of Mn:$Cs_2NaTbCl_6$ can be continuously tuned from green to red. The PLQY of the samples first increases and then decreases as Mn^{2+}-feeding concentration increases, and the sample with 3% Mn^{2+}-feeding concentration has the highest PLQY of 52.6% (Figure S6a−f).

The PL decay spectra of x%Mn:$Cs_2NaTbCl_6$ (x = 0, 0.5, 1, 2, 3, 5) at 548 and 622 nm (λ_{ex} = 278 nm) are shown in Figure 3c and 3f, respectively. The fitting values of PL decay profiles are summarized in Tables S1 and S2, and both emissions from Tb^{3+} and Mn^{2+} exhibit millisecond-scale lifetimes corresponding to the d−f transition of Tb^{3+} and d−d transition of Mn^{2+}. Upon increasing the Mn^{2+}-doping concentration, the PL lifetime of Tb^{3+} intrinsic emission at 548 nm decreases from 5.12 to 1.74 ms, while the PL lifetime of Mn^{2+} emission at 622 nm increases from 5.10 to 13.28 ms. The relationship between the lifetimes of double emission and the Mn^{2+}-feeding concentration is shown in Figure S7. The lifetime of Tb^{3+} emission decreases slightly as the Mn^{2+}-feeding concentration increases, while the lifetime of Mn^{2+} emission increases, which confirms the energy transfer process from Tb^{3+} to Mn^{2+}. Thus, increasing Mn^{2+}-doping concentration promotes the energy transfer from the $^5D_4$ of Tb^{3+} to $^4T_1$ of Mn^{2+} in Mn-doped $Cs_2NaTbCl_6$.

Figure 4a shows the temperature-dependent PL spectra of 3%Mn:$Cs_2NaTbCl_6$ from 100 to 360 K. Figure S8a is pseudocolor map from 100 to 360 K. Figure S8b and c are obtained from Figures 4a and S8a, and Figure S8b shows the evolution of the double emission with temperature. The PL position of Tb^{3+} is independent of temperature due to the fact that the d−f transition emission of rare-earths is relatively insensitive to the temperature, but that of Mn^{2+} shows a continuous blue shift with increasing temperature attributing to decrease in crystal-field strength and the spin−spin coupling energy caused by thermal expansion of the host lattice at elevated temperature.[49,50] Figure 4b shows a change of the intensity of the double emission with temperature. The PL intensity from Tb^{3+} and Mn^{2+} ions decreases gradually upon increasing temperature from 100 to 240 K, which is mainly caused by thermal quenching due to electron−phonon coupling. From 240 to 360 K, the PL intensity of Mn^{2+} still continues to decrease, while the PL intensity of Tb^{3+} gradually increases. Finally, when the temperature reaches 360 K, the intensity of PL peaks at 548 and 622 nm remains at 84% and 66% of the value at 100 K, respectively, exhibiting excellent antithermal quenching behavior. Figure S8c is a Boltzmann analysis of the Mn^{2+} emission intensity as a function of temperatures (T = 220−360 K), and the sensitization activation energy ΔE_S at 220 K can be calculated by eq 1:[51,52]

$$I_{Mn}(T) = I_0 e^{-\Delta E_S/k_B T} \quad (1)$$

where $I_{Mn}(T)$ is the integrated PL intensity at temperature T (K), and k_B is the Boltzmann constant. The Boltzmann analysis through the expression yields a sensitization activation energy ΔE_S (90.8 meV) of 220 K, which is much larger than the thermal energy of 19.2 meV ($k_B T_{T=220\ K}$). Such a large potential barrier is not conducive to intersystem crossing of electrons in the relative high temperature range, resulting in a decrease of Mn^{2+} emission. Instead, most of the electrons are stranded in the $^5D_4$ energy level of Tb^{3+}, and return the ground state in the form of $^5D_4 \rightarrow {}^7F_5$ transitions, which eliminates the effect of thermal quenching at 548 nm and enhance intrinsic luminescence. Figure 4c and d are the PL decay profiles for the 548 and 622 nm emissions, respectively. The PL lifetimes at 100−360 K are summarized in Tables S3 and S4. All the PL decay dynamics can be well fitted with a biexponential function. Figure 4e shows the lifetime evolution of dual emission with temperature in 100−360 K. From 100−220 K, the lifetimes of Tb^{3+} and Mn^{2+} emission decrease as the

https://doi.org/10.1021/acs.jpclett.2c02491
J. Phys. Chem. Lett. 2022, 13, 8529−8536

temperature increases. However, in the 220−360 K region, the PL lifetime of Mn^{2+} ion still decreases gradually, while the PL lifetime of Tb^{3+} ion emission increases gradually. This seems to suggest that electrons transfer from Tb^{3+} to Mn^{2+} is inefficient in the relative high temperature range. Meanwhile, we can also roughly describe the transfer and recombination efficiency of electrons by the energy transfer efficiency. The energy transfer efficiency η_T in 3%Mn:$Cs_2NaTbCl_6$ at different temperature can be calculated by eq 2:[44,53,54]

$$\eta_T = 1 - \frac{\tau_x}{\tau_0} \tag{2}$$

where τ_0 and τ_x are the PL lifetimes of undoped and doped samples at 548 nm at different temperature. The calculated results are shown in Table S5. The energy transfer efficiency increases from 27.94% to 43.62% as the temperature increases from 100 to 220 K. When the temperature continues to increase, the energy transfer efficiency decreases gradually, and at 340 K the efficiency decreases to 33.58%. Thus, this further confirms that the increase in PL intensity of Tb^{3+} at 548 nm from 240−360 K is due to the decrease in the efficiency of energy transfer from Tb^{3+} to Mn^{2+}, which eliminates the negative effect of thermal quenching.

A schematic illustration of the photophysical processes of Mn:$Cs_2NaTbCl_6$ is shown in Figure 4f. Under the excitation of 278 nm light, electrons not only can relax through the host intrinsic Tb^{3+} $^5D_4 \rightarrow {}^7F_{J=6,5,4,3}$ transition but also can intersystem cross to the d-state of Mn^{2+} and relax through the $^4T_1 \rightarrow {}^6A_1$ transition, thus the tunable double emission observed. As mentioned earlier, the energy transfer from Tb^{3+} to Mn^{2+} is gradually enhanced with increasing Mn^{2+}-feeding concentration, leading to higher population of the $^4T_1$ state of Mn^{2+} and increasing red emission. Meanwhile, as shown in Figure S9a−c, the Mn^{2+} emission red-shifts with increasing Mn^{2+}-feeding concentration, indicating that Mn−Mn interactions may exist in the highly doped system, resulting in reduction and red-shift of $^4T_1 \rightarrow {}^6A_1$ Mn^{2+} emission.

The stability of the samples was studied as a function of storage time under ambient conditions. Figure 5a shows the XRD patterns of the obtained 3%Mn:$Cs_2NaTbCl_6$ crystals after being stored in the air (RT: 25−27 °C; RH: 50−70%) for one month. The diffraction intensity of NaCl is increased, but the overall diffraction peaks remain almost unchanged, which indicate that the sample is slightly decomposed. In Figure 5b, the PL intensity of 3%Mn:$Cs_2NaTbCl_6$ still remains about 90% of the initial value after being stored one month in the air. As shown in Figure 5h, thermogravimetric analysis (TGA) indicates that the decomposition temperature of pristine $Cs_2NaTbCl_6$ and 3%Mn:$Cs_2NaTbCl_6$ is about 767 and 770 °C, respectively, which suggests that Mn doping does not obviously affect the thermal stability of $Cs_2NaTbCl_6$. High decomposition temperature suggests that these kinds of rare-earth double perovskites should be excellent candidates for the photoelectric applications in the future.

Furthermore, we fabricated LEDs based on 3% Mn:$Cs_2NaTbCl_6$. As shown in Figure 5c−f, the PL spectra of all LEDs show excellent spectral stability at different voltages and currents. Figure 5g shows the photographs of the working green LED prepared based on pristine $Cs_2NaTbCl_6$ under 3.5 V driving voltage and the working orange LED prepared based on 3%Mn:$Cs_2NaTbCl_6$ under 5.5 V driving voltage, respectively. The green LED exhibited bright PL with chromaticity coordinate (CIE) of (0.308, 0.575) and correlated color temperature (CCT) of 5958 K. The orange LED exhibited bright PL with CIE of (0.579, 0.352) and CCT of 2547 K. This indicates that these rare-earth double perovskites have promising applications in optoelectronic fields such as solid-state lighting.

In summary, novel Mn^{2+}-doped $Cs_2NaTbCl_6$ rare-earth double perovskites were synthesized by the solvothermal method and found to show interesting tunable dual emission and excellent stability. Based on experimental results and theoretical calculations, the mechanism of Mn^{2+} doping is proposed to first insert into the interstitial void when Mn-feeding concentrations is lower than 1%, but when the Mn-feeding concentration exceeds 1%, Mn^{2+} will further substitute Na^+ site of the $Cs_2NaTbCl_6$ lattice, and thus, both two doping modes coexist with the interstitial doping. Further, the emission color could be modulated from green to red because energy transfer could be effectively achieved from $^5D_4$ level of Tb^{3+} ions to $^4T_1$ level of Mn^{2+} ions by increasing the Mn^{2+}-feeding concentration. Further, prototype LEDs based on these double perovskites show good performance. This study provides new insight into the competitive energy transfer processes in luminescent doped metal halide double perovskites.

■ ASSOCIATED CONTENT

Supporting Information

The Supporting Information is available free of charge at https://pubs.acs.org/doi/10.1021/acs.jpclett.2c02491.

Detailed description of experimental synthesis, first principle calculation and additional data including relaxed structures, XPS spectra, EDS-mapping, PL spectra, PLE spectra, PLQYs, PL lifetime, band-structure, etc. (PDF)

■ AUTHOR INFORMATION

Corresponding Authors

Ruosheng Zeng − *School of Physical Science and Technology, MOE Key Laboratory of New Processing Technology for Non-ferrous Metals and Materials, Guangxi Key Laboratory of Processing for Non-ferrous Metals and Featured Materials, Guangxi University, Nanning 530004, China;* orcid.org/0000-0002-8536-326X; Email: zengrsh@guet.edu.cn

Jin Zhong Zhang − *Department of Chemistry and Biochemistry, University of California, Santa Cruz, California 95064, United States*; Email: zhang@ucsc.edu

Authors

Yuanjie Chen − *School of Physical Science and Technology, MOE Key Laboratory of New Processing Technology for Non-ferrous Metals and Materials, Guangxi Key Laboratory of Processing for Non-ferrous Metals and Featured Materials, Guangxi University, Nanning 530004, China*

Qilin Wei − *School of Physical Science and Technology, MOE Key Laboratory of New Processing Technology for Non-ferrous Metals and Materials, Guangxi Key Laboratory of Processing for Non-ferrous Metals and Featured Materials, Guangxi University, Nanning 530004, China*

Shuai Zhang − *School of Physical Science and Technology, MOE Key Laboratory of New Processing Technology for Non-ferrous Metals and Materials, Guangxi Key Laboratory of Processing for Non-ferrous Metals and Featured Materials, Guangxi University, Nanning 530004, China*

https://doi.org/10.1021/acs.jpclett.2c02491
J. Phys. Chem. Lett. 2022, 13, 8529−8536

Binbin Luo − *Department of Chemistry and Key Laboratory for Preparation and Application of Ordered Structural Materials of Guangdong Province, Shantou University, Shantou, Guangdong 515063, China;* orcid.org/0000-0001-9652-7998

Canxu Chen − *School of Physical Science and Technology, MOE Key Laboratory of New Processing Technology for Non-ferrous Metals and Materials, Guangxi Key Laboratory of Processing for Non-ferrous Metals and Featured Materials, Guangxi University, Nanning 530004, China*

Xiaoshan Zhu − *Department of Electrical and Biomedical Engineering, University of Nevada Reno, Reno, Nevada 89557, United States*

Sheng Cao − *School of Physical Science and Technology, MOE Key Laboratory of New Processing Technology for Non-ferrous Metals and Materials, Guangxi Key Laboratory of Processing for Non-ferrous Metals and Featured Materials, Guangxi University, Nanning 530004, China;* orcid.org/0000-0002-6203-9088

Bingsuo Zou − *School of Physical Science and Technology, MOE Key Laboratory of New Processing Technology for Non-ferrous Metals and Materials, Guangxi Key Laboratory of Processing for Non-ferrous Metals and Featured Materials, Guangxi University, Nanning 530004, China;* orcid.org/0000-0003-4561-4711

Complete contact information is available at: https://pubs.acs.org/10.1021/acs.jpclett.2c02491

Notes

The authors declare no competing financial interest.

■ ACKNOWLEDGMENTS

This work was supported by the National Natural Science Foundation of China (Grant Nos. 22175043, 52162021) and Guangxi Natural Science Foundation (Grant No. 2017GXNSFGA198005). J.Z.Z. is grateful to the US NSF for financial support (CHE-2203633). B.L. thanks the financial support from the Open Foundation of Guangxi Key Laboratory of Processing for Nonferrous Metals and Featured Materials (Grant No. 2022GXYSOF14). The calculation was conducted using the high-performance computing platform of Guangxi University.

■ REFERENCES

(1) Guo, X.; Zhao, B.; Xu, K.; Yang, S.; Liu, Z.; Han, Y.; Xu, J.; Xu, D.; Tan, Z.; Liu, S. F. p-Type carbon dots for effective surface optimization for near-record-efficiency $CsPbI_2Br$ solar cells. *Small* **2021**, *17* (37), 2102272.

(2) Gao, Y.; Xu, W.; He, F.; Nie, P.; Yang, Q.; Si, Z.; Meng, H.; Wei, G. Carbon nanodots enhanced performance of $Cs_{0.15}FA_{0.85}PbI_3$ perovskite solar cells. *Nano Research* **2021**, *14* (7), 2294−2300.

(3) Chen, Y.; Zuo, X.; He, Y.; Qian, F.; Zuo, S.; Zhang, Y.; Liang, L.; Chen, Z.; Zhao, K.; Liu, Z.; Gou, J.; Liu, S. F. Dual passivation of perovskite and SnO_2 for high-efficiency $MAPbI_3$ perovskite solar cells. *Advanced Science* **2021**, *8* (5), 2001466.

(4) Lin, K.; Yan, C.; Sabatini, R. P.; Feng, W.; Lu, J.; Liu, K.; Ma, D.; Shen, Y.; Zhao, Y.; Li, M.; Tian, C.; Xie, L.; Sargent, E. H.; Wei, Z. Dual-phase regulation for high-efficiency perovskite light-emitting diodes. *Adv. Funct. Mater.* **2022**, *32* (24), 2200350.

(5) Wang, Z.; Fu, R.; Li, F.; Xie, H.; He, P.; Sha, Q.; Tang, Z.; Wang, N.; Zhong, H. One-step polymeric pelt encapsulation method to prepare $CsPbBr_3$ perovskite quantum dots/polymethyl methacrylate composite with high performance. *Adv. Funct. Mater.* **2021**, *31* (22), 2010009.

(6) Pang, P.; Jin, G.; Liang, C.; Wang, B.; Xiang, W.; Zhang, D.; Xu, J.; Hong, W.; Xiao, Z.; Wang, L.; Xing, G.; Chen, J.; Ma, D. Rearranging low-dimensional phase distribution of Quasi-2D perovskites for efficient sky-blue perovskite light-emitting diodes. *ACS Nano* **2020**, *14* (9), 11420−11430.

(7) Ren, M.; Cao, S.; Zhao, J.; Zou, B.; Zeng, R. Advances and challenges in two-dimensional organic−inorganic hybrid perovskites toward high-performance light-emitting diodes. *Nano-Micro Letters* **2021**, *13* (1), 163.

(8) Lei, L.; Dong, Q.; Gundogdu, K.; So, F. Metal halide perovskites for laser applications. *Adv. Funct. Mater.* **2021**, *31* (16), 2010144.

(9) Xu, Y.; Chen, Q.; Zhang, C.; Wang, R.; Wu, H.; Zhang, X.; Xing, G.; Yu, W. W.; Wang, X.; Zhang, Y.; Xiao, M. Two-photon-pumped perovskite semiconductor nanocrystal lasers. *J. Am. Chem. Soc.* **2016**, *138* (11), 3761−3768.

(10) Jin, M.; Gao, W.; Liang, X.; Fang, Y.; Yu, S.; Wang, T.; Xiang, W. The achievement of red upconversion lasing for highly stable perovskite nanocrystal glasses with the assistance of anion modulation. *Nano Research* **2021**, *14* (8), 2861−2866.

(11) Du, X.; Liu, Y.; Pan, W.; Pang, J.; Zhu, J.; Zhao, S.; Chen, C.; Yu, Y.; Xiao, Z.; Niu, G.; Tang, J. Chemical potential diagram guided rational tuning of electrical properties: a case study of $CsPbBr_3$ for X-ray detection. *Adv. Mater.* **2022**, *34* (17), 2110252.

(12) Di, J.; Li, H.; Su, J.; Yuan, H.; Lin, Z.; Zhao, K.; Chang, J.; Hao, Y. Reveal the humidity effect on the phase pure $CsPbBr_3$ single crystals formation at room temperature and its application for ultrahigh sensitive X-ray detector. *Advanced Science* **2022**, *9* (2), 2103482.

(13) Chen, D.; Huang, D.; Yang, M.; Xu, K.; Hu, J.; Xu, F.; Liang, S.; Zhu, H. Room-temperature direct synthesis of tetragonal β-$CsPbI_3$ nanocrystals. *Advanced Optical Materials* **2022**, *10* (2), 2101869.

(14) Wu, X.; Guo, Z.; Zhu, S.; Zhang, B.; Guo, S.; Dong, X.; Mei, L.; Liu, R.; Su, C.; Gu, Z. Ultrathin, transparent, and high density perovskite scintillator film for high resolution X-ray microscopic imaging. *Advanced Science* **2022**, *9*, 2200831.

(15) Ma, W.; Jiang, T.; Yang, Z.; Zhang, H.; Su, Y.; Chen, Z.; Chen, X.; Ma, Y.; Zhu, W.; Yu, X.; Zhu, H.; Qiu, J.; Liu, X.; Xu, X.; Yang, Y. M. Highly resolved and robust dynamic X-ray imaging using perovskite glass-ceramic scintillator with reduced light scattering. *Advanced Science* **2021**, *8* (15), 2003728.

(16) Huang, H.; Bodnarchuk, M. I.; Kershaw, S. V.; Kovalenko, M. V.; Rogach, A. L. Lead halide perovskite nanocrystals in the research spotlight: stability and defect tolerance. *ACS Energy Letters* **2017**, *2* (9), 2071−2083.

(17) Swarnkar, A.; Mir, W. J.; Nag, A. Can B-Site doping or alloying improve thermal- and phase-stability of all-inorganic $CsPbX_3$ (X = Cl, Br, I) perovskites? *ACS Energy Letters* **2018**, *3* (2), 286−289.

(18) Ren, J.; Zhou, X.; Wang, Y. Water triggered interfacial synthesis of highly luminescent $CsPbX_3$:Mn^{2+} quantum dots from non-luminescent quantum dots. *Nano Research* **2020**, *13* (12), 3387−3395.

(19) Babayigit, A.; Ethirajan, A.; Muller, M.; Conings, B. Toxicity of organometal halide perovskite solar cells. *Nat. Mater.* **2016**, *15* (3), 247−251.

(20) Lin, Y.; Hu, S.; Xia, B.; Fan, K.; Gong, L.; Kong, J.; Huang, X.; Xiao, Z.; Du, K. Material design and optoelectronic properties of three-dimensional quadruple perovskite halides. *J. Phys. Chem. Lett.* **2019**, *10* (17), 5219−5225.

(21) De Angelis, F. The prospect of lead-free perovskite photovoltaics. *ACS Energy Letters* **2021**, *6* (4), 1586−1587.

(22) Xiao, Z.; Song, Z.; Yan, Y. From lead halide perovskites to lead-free metal halide perovskites and perovskite derivatives. *Adv. Mater.* **2019**, *31* (47), 1803792.

(23) Xiao, Z.; Meng, W.; Wang, J.; Mitzi, D. B.; Yan, Y. Searching for promising new perovskite-based photovoltaic absorbers: the importance of electronic dimensionality. *Materials Horizons* **2017**, *4* (2), 206−216.

(24) Zeng, R.; Bai, K.; Wei, Q.; Chang, T.; Yan, J.; Ke, B.; Huang, J.; Wang, L.; Zhou, W.; Cao, S.; Zhao, J.; Zou, B. Boosting triplet self-

trapped exciton emission in Te(IV)-doped Cs_2SnCl_6 perovskite variants. *Nano Research* **2021**, *14* (5), 1551−1558.
(25) Zhu, T.; Yang, Y.; Gong, X. Recent advancements and challenges for low-toxicity perovskite materials. *ACS Appl. Mater. Interfaces* **2020**, *12* (24), 26776−26811.
(26) Shao, S.; Liu, J.; Portale, G.; Fang, H.; Blake, G. R.; Ten Brink, G. H.; Koster, L. J. A.; Loi, M. A. Highly reproducible Sn-rased hybrid perovskite solar cells with 9% efficiency. *Adv. Energy Mater.* **2018**, *8* (4), 1702019.
(27) Arfin, H.; Kshirsagar, A. S.; Kaur, J.; Mondal, B.; Xia, Z.; Chakraborty, S.; Nag, A. ns^2 Electron (Bi^{3+} and Sb^{3+}) doping in lead-free metal halide perovskite derivatives. *Chem. Mater.* **2020**, *32* (24), 10255−10267.
(28) Yan, J.; Zhang, S.; Wei, Q.; Cao, S.; Zhao, J.; Zou, B.; Zeng, R. Stoichiometry-controlled phase engineering of cesium bismuth halides and reversible structure switch. *Advanced Optical Materials* **2022**, *10* (5), 2101406.
(29) Huang, J.; Chang, T.; Zeng, R.; Yan, J.; Wei, Q.; Zhou, W.; Cao, S.; Zou, B. Controlled structural transformation in Sb-doped indium halides A_3InCl_6 and $A_2InCl_5{\bullet}H_2O$ yields reversible green-to-yellow emission switch. *Advanced Optical Materials* **2021**, *9* (13), 2002267.
(30) Shil, S. K.; Wang, F.; Lai, Z.; Meng, Y.; Wang, Y.; Zhao, D.; Hossain, M. K.; Egbo, K. O.; Wang, Y.; Yu, K. M.; Ho, J. C. Crystalline all-inorganic lead-free $Cs_3Sb_2I_9$ perovskite microplates with ultra-fast photoconductive response and robust thermal stability. *Nano Research* **2021**, *14* (11), 4116−4124.
(31) Igbari, F.; Wang, Z.; Liao, L. Progress of lead-free halide double perovskites. *Adv. Energy Mater.* **2019**, *9* (12), 1803150.
(32) Lei, H.; Hardy, D.; Gao, F. Lead-free double perovskite $Cs_2AgBiBr_6$: fundamentals, applications, and perspectives. *Adv. Funct. Mater.* **2021**, *31* (49), 2105898.
(33) Liu, Y.; Nag, A.; Manna, L.; Xia, Z. Lead-free double perovskite $Cs_2AgInCl_6$. *Angew. Chem., Int. Ed.* **2021**, *60* (21), 11592−11603.
(34) Luo, J.; Li, S.; Wu, H.; Zhou, Y.; Li, Y.; Liu, J.; Li, J.; Li, K.; Yi, F.; Niu, G.; Tang, J. $Cs_2AgInCl_6$ double perovskite single crystals: parity forbidden transitions and their application for sensitive and fast UV photodetectors. *ACS Photonics* **2018**, *5* (2), 398−405.
(35) Liao, Q.; Meng, Q.; Jing, L.; Pang, J.; Pang, Q.; Zhang, J. Z. Highly emissive and table $Cs_2AgInCl_6$ double perovskite nanocrystals by Bi^{3+} doping and potassium bromide surface passivation. *J. Phys. Chem. C* **2021**, *125* (33), 18372−18379.
(36) Meng, Q.; Zhou, L.; Pang, Q.; He, X.; Wei, T.; Zhang, J. Z. Enhanced photoluminescence of all-inorganic manganese halide perovskite-analogue nanocrystals by lead ion incorporation. *J. Phys. Chem. Lett.* **2021**, *12* (41), 10204−10211.
(37) Sun, Y.; Fernández-Carrión, A. J.; Liu, Y.; Yin, C.; Ming, X.; Liu, B.; Wang, J.; Fu, H.; Kuang, X.; Xing, X. Bismuth-based halide double perovskite $Cs_2LiBiCl_6$: crystal structure, luminescence, and stability. *Chem. Mater.* **2021**, *33* (15), 5905−5916.
(38) Zeng, R.; Zhang, L.; Xue, Y.; Ke, B.; Zhao, Z.; Huang, D.; Wei, Q.; Zhou, W.; Zou, B. Highly efficient blue emission from self-trapped excitons in stable Sb^{3+}-doped $Cs_2NaInCl_6$ double perovskites. *J. Phys. Chem. Lett.* **2020**, *11* (6), 2053−2061.
(39) Zhang, L.; Xie, X.; Li, D.; Yuan, Y.; Xue, X.; Li, Q.; Xu, J.; Wang, H.; Hu, F.; Zhang, X. Investigation on lead-free Mn-doped $Cs_2NaInCl_6$ double perovskite phosphors and their optical properties. *Opt. Mater.* **2021**, *122*, 111802.
(40) Majher, J. D.; Gray, M. B.; Strom, T. A.; Woodward, P. M. $Cs_2NaBiCl_6$:Mn^{2+}—a new orange-red halide double perovskite phosphor. *Chem. Mater.* **2019**, *31* (5), 1738−1744.
(41) Saikia, S.; Joshi, A.; Arfin, H.; Badola, S.; Saha, S.; Nag, A. Sb^{3+}−Er^{3+}-codoped $Cs_2NaInCl_6$ for emitting blue and short-wave infrared radiation. *Angew. Chem., Int. Ed.* **2022**, *61* (32), No. e202201628.
(42) Cheng, X.; Xie, Z.; Zheng, W.; Li, R.; Deng, Z.; Tu, D.; Shang, X.; Xu, J.; Gong, Z.; Li, X.; Chen, X. Boosting the self-trapped exciton emission in alloyed $Cs_2(Ag/Na)InCl_6$ double perovskite via Cu^+ doping. *Advanced Science* **2022**, *9* (7), 2103724.
(43) Huang, A.; Duan, C.; Wong, K.; Tanner, P. A. Downshifting in $Cs_2NaBiCl_6$:Er^{3+}: transforming ultraviolet into near infrared radiation. *Journal of Materials Chemistry C* **2022**, *10* (8), 2950−2954.
(44) Liu, Y.; Rong, X.; Li, M.; Molokeev, M. S.; Zhao, J.; Xia, Z. Incorporating rare-earth terbium(III) ions into $Cs_2AgInCl_6$:Bi nanocrystals toward tunable photoluminescence. *Angew. Chem., Int. Ed.* **2020**, *59* (28), 11634−11640.
(45) Chen, N.; Cai, T.; Li, W.; Hills-Kimball, K.; Yang, H.; Que, M.; Nagaoka, Y.; Liu, Z.; Yang, D.; Dong, A.; Xu, C.; Zia, R.; Chen, O. Yb^- and Mn^-doped lead-free double perovskite Cs_2AgBiX_6 (X = Cl−, Br−) nanocrystals. *ACS Appl. Mater. Interfaces* **2019**, *11* (18), 16855−16863.
(46) Arfin, H.; Kaur, J.; Sheikh, T.; Chakraborty, S.; Nag, A. Bi^{3+}-Er^{3+} and Bi^{3+}-Yb^{3+} codoped $Cs_2AgInCl_6$ double perovskite near-infrared emitters. *Angew. Chem., Int. Ed.* **2020**, *59* (28), 11307−11311.
(47) Zhang, R.; Wang, Z.; Xu, X.; Mao, X.; Xiong, J.; Yang, Y.; Han, K. All-Inorganic rare-earth halide double perovskite single crystals with highly efficient photoluminescence. *Advanced Optical Materials* **2021**, *9* (19), 2100689.
(48) Wei, Q.; Lin, C.; Li, Y.; Zhang, X.; Zhang, Q.; Shen, Q.; Cheng, Y.; Huang, W. Physics of intrinsic point defects in bismuth oxychalcogenides: a first-principles investigation. *J. Appl. Phys.* **2018**, *124*, No. 055701.
(49) Yuan, X.; Ji, S.; De Siena, M. C.; Fei, L.; Zhao, Z.; Wang, Y.; Li, H.; Zhao, J.; Gamelin, D. R. Photoluminescence temperature dependence, dynamics, and quantum efficiencies in Mn^{2+}-doped $CsPbCl_3$ perovskite nanocrystals with varied dopant concentration. *Chem. Mater.* **2017**, *29* (18), 8003−8011.
(50) Wang, S.; Han, X.; Kou, T.; Zhou, Y.; Liang, Y.; Wu, Z.; Huang, J.; Chang, T.; Peng, C.; Wei, Q.; Zou, B. Lead-free Mn^{II}-based red-emitting hybrid halide $(CH_6N_3)_2MnCl_4$ toward high performance warm WLEDs. *Journal of Materials Chemistry C* **2021**, *9* (14), 4895−4902.
(51) Wei, J.; Liao, J.; Wang, X.; Zhou, L.; Jiang, Y.; Kuang, D. All-inorganic lead-free heterometallic $Cs_4MnBi_2Cl_{12}$ perovskite single crystal with highly efficient orange emission. *Matter* **2020**, *3* (3), 892−903.
(52) Luo, B.; Guo, Y.; Li, X.; Xiao, Y.; Huang, X.; Zhang, J. Z. Efficient trap-mediated Mn^{2+} dopant emission in two dimensional single-layered perovskite $(CH_3CH_2NH_3)_2PbBr_4$. *J. Phys. Chem. C* **2019**, *123* (23), 14239−14245.
(53) Zhou, G.; Jiang, X.; Molokeev, M.; Lin, Z.; Zhao, J.; Wang, J.; Xia, Z. Optically modulated ultra-broad-band warm white emission in Mn^{2+}-doped $(C_6H_{18}N_2O_2)PbBr_4$ hybrid metal halide phosphor. *Chem. Mater.* **2019**, *31* (15), 5788−5795.
(54) Nie, J.; Li, H.; Fang, S.; Zhou, B.; Liu, Z.; Chen, F.; Wang, Y.; Shi, Y. Efficient red photoluminescence in holmium-doped $Cs_2NaInCl_6$ double perovskite. *Cell Reports Physical Science* **2022**, *3* (4), 100820.

https://doi.org/10.1021/acs.jpclett.2c02491
J. Phys. Chem. Lett. 2022, 13, 8529−8536